

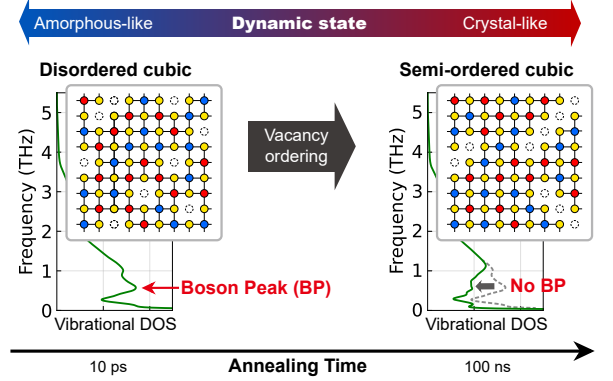
Study of vacancy ordering and the boson peak in metastable cubic Ge-Sb-Te using machine learning potentials

Young-Jae Choi, Minjae Ghim, and Seung-Hoon Jhi*

Department of Physics, Pohang University of Science and Technology, Pohang 37673, Republic of Korea

(Dated: January 5, 2024)

The mechanism of the vacancy ordering in metastable cubic Ge-Sb-Te (c-GST) that underlies the ultrafast phase-change dynamics and prominent thermoelectric properties remains elusive. Achieving a comprehensive understanding of the vacancy-ordering process at an atomic level is challenging because of enormous computational demands required to simulate disordered structures on large temporal and spatial scales. In this study, we investigate the vacancy ordering in c-GST by performing large-scale molecular dynamics simulations using machine learning potentials. The initial c-GST structure with randomly distributed vacancies rearranges to develop a semi-ordered cubic structure with layer-like ordered vacancies after annealing at 700 K for 100 ns. The vacancy ordering significantly affects the lattice dynamical properties of c-GST. In the initial structure with fully disordered vacancies, we observe a boson peak, usually associated with amorphous solids, that consists of localized modes at ~ 0.575 THz. The boson peak modes are highly localized around specific atomic arrangements of straight vacancy-Te-vacancy trios. As vacancies become ordered, the boson peak disappears, and the Debye-Waller thermal B factor of Te decreases substantially. This finding indicates that the c-GST undergoes a transition from amorphous-like to crystalline-like solid state by thermal annealing in low-frequency dynamics.



I. INTRODUCTION

Chalcogen-based phase-change materials are considered promising candidates for next-generation non-volatile memory devices [1–3]. Ge-Sb-Te (GST) ternary compounds especially have attracted great attention due to the high stability of their amorphous solid phase and the convenient phase-switching operations by either electric, thermal, or laser pulses [2]. While GeTe exhibits a drastic change in resistivity ($\sim 10^6$ fold) by the amorphous to crystalline phase transition at $T \sim 450$ K, crystalline GST displays a multilevel resistivity spectrum over a 1000-fold range when annealed at $400 \text{ K} < T < 600 \text{ K}$ [4]. Amorphous GST (a-GST) crystallizes into a metastable rock-salt cubic phase (c-GST) before further crystallizing into a hexagonal phase (h-GST). In c-GST lattice structures, anions (Te) occupy 4a sublattice sites, while cations (Ge/Sb) and vacancies occupy 4b sites [5]. Stable h-GST, obtainable by high-temperature annealing at $T > 500$ K, has a layered structure with alternating stacks of anion and cation layers [4]. Several types of hexagonal phases are distinguished by the sequence of layer stacking, with the most stable and commonly observed being the Kooi sequence (vacancy-Te-Sb-Te-Ge-Te-Ge-Te-Sb-Te) [6].

GST phase-change memory devices exhibit fast amorphous to crystalline phase switching by electric pulses,

which occur within 100 ns [3]. A few models have been proposed as a microscopic origin of the rapid crystallization of GST. Kolobov *et al.* proposed that the rapid phase transition of GST is possible by the facile transfer of cations from a tetrahedron center in its amorphous state to an octahedron center in its cubic state, namely the umbrella-flip distortion model [7]. Hegedüs and Elliott conducted *ab-initio* molecular dynamics (AIMD) simulations of the amorphous-to-cubic phase transition in a 63-atom $\text{Ge}_2\text{Sb}_2\text{Te}_5$ (GST225) system and found that the fast crystallization of a-GST was caused by the excessive formation of 4-fold rings by melt-quenching [8]. The growth rate of a GST crystal domain is also fast, ranging $10^{-9} \sim 3$ m/s, depending on the annealing temperature [9, 10]. Lee and Elliott [11] demonstrated, through an AIMD annealing simulation of a 180-atom a-GST system, that vacancies located near amorphous-crystal interfaces may promote the rapid growth of a crystal domain. Recently, the change in electronic structure by crystallization was investigated using the maximally localized Wannier function method from a large-scale AIMD simulation of a 328-atom system [12]. The complex configuration of Wannier electrons in a-GST, including many weak bonding states and lone-pair electrons, is advantageous for the fast structural transition accompanied by frequent bond-breaking and formation processes [12].

The a-GST structures build s - p hybridized covalent bonding states, while well-ordered crystalline structures build directional p -orbital resonant bonding states, which leads to a stark optical contrast between the two struc-

* jhish@postech.ac.kr

tures [13]. The directional p -bonding could become unstable against sp^3 bonding as the p -bonding chain length increases [14]. A signature of the p -bonding instability is the softening of specific phonon modes, resulting in the distortion observed in α -GeTe with alternating long and short bonds [15]. In this sense, the presence of vacancies can stabilize the p -bonding chains, and their distribution is a key for understanding the structural and electronic properties of c-GST.

The distribution of vacancies in c-GST can be either random or ordered to a certain degree [16]. The vacancy-ordered-cubic (VOC) structures slightly differ from the hexagonal structures in terms of interlayer distance and stacking geometry of Te-Te van der Waals (vdW) layers [16]. A typical hexagonal structure obtained by annealing is the Matsunaga phase, which is similar to the Kooi phase but with numerous substitutional defects of Ge and Sb atoms [17]. A major structural change in the cubic-to-hexagonal phase transition is thus accompanied by vacancy ordering. The electrical resistance of crystalline GST, which varies over a 1000-fold range, reflects vacancy ordering and exhibits a feature of the metal-insulator transition at a certain threshold [4]. Additionally, GST-based phase-change memories show a reduction in crystallization temperature and electrical resistance with an increase in operation cycles [10]. A non-Arrhenius crystallization of a-GST was observed, as the activation energy underwent a discontinuous 6-fold magnitude change at $T \sim 480$ K [10]. All these observations in phase-change memories are likely attributed to the distribution of vacancies and their ordering. However, they cannot be tracked atomistically by measurements nor by first-principles simulations due to their complexity in length and time scales.

The atomic-scale studies of GST on electronic and structural properties require a substantial size in atomic number and simulation time. Direct AIMD simulations are limited to ~ 1000 atoms due to high computational costs [18–22]. Recently, machine learning potential (MLP) methods have expanded the simulation capacity to an unreachable scale by AIMD, allowing atomistic calculations with an accuracy of first-principles methods [23–26]. The medium-range order of large-sized ring configurations has been identified and the first sharp diffraction peak of X-ray structure factor in measurement has been reproduced [23]. The mid-gap states in amorphous GST225 [24] and quench-rate-dependent crystallization [25] have also been directly addressed in machine-learning-potential molecular dynamics (MLMD) without resort to phenomenological modeling. In this study, we used MLMD methods to simulate the thermal annealing of c-GST at 700 K and analyzed the distribution and rearrangement of vacancies.

II. METHODS

A. $\text{Ge}_2\text{Sb}_2\text{Te}_5$ potential

We utilized the Neural E(3)-equivariant interatomic potentials (NequIP) model to develop MLPs for GST225 [27]. NequIP is based on graph neural networks and learns a high-dimensional potential energy surface by partitioning the potential energy of a system into individual atomic contributions, namely atomic energies [27]. The NequIP process involves multiple iterations of message passing to effectively convey non-local structural information [27]. The message passing operates with feature tensors that contain structural information and are equivariant under rotation, reflection, and translation transformations [27].

The NequIP potential was constructed with a local cutoff radius r_c of 4 Å, including 7.40 atoms on average inside a local environment sphere. The maximum rotation order l_{max} of the feature tensors was set to be 3, as the potentials with $l_{\text{max}}=3$ reproduce the angular distribution function of liquid GST225 at 1100 K better than those with $l_{\text{max}}=2$ (see Supplemental Material for further information on the NequIP training parameters [28]). The converged GST225 potentials yielded an energy root-mean-square error (RMSE) of 51.8 meV/atom and a force RMSE of 74.7 meV/Å for the whole validation dataset. We note that the RMSE values can vary consequentially for each class of the training dataset. For the c-GST dataset, which is the primarily focused phase of this study, the RMSEs are 33.8 meV/atom for energies and 43.8 meV/Å for forces (see Supplemental Material for the validation of the GST225 potential [28]). Inclusion of a dataset in a wider energy window inevitably increases the RMSEs but covers the potential energy surface more broadly, ensuring more vigorous stability of molecular dynamics simulations [29].

The resulting GST225 potentials simulated properly the melting and crystallization processes (see Supplemental Material for the potential energy change during melting and crystallization [28]). The melting point of c-GST in our simulation was found to be ~ 1000 K, which is comparable to the measurement of ~ 900 K [30]. A slight discrepancy may be attributed to some factors neglected in our simulations such as surfaces or structural defects that accelerate the melting process. The amorphous-to-cubic crystallization time was estimated to be about 400~700 ps, which is similar to the results in previous studies (400~600 ps) using a different type of MLP [23].

B. Randomized Atomic-system Generator (RAG)

To develop the GST225 potentials, we constructed a training dataset using the randomized atomic-system generator (RAG) method [29]. The RAG is a novel approach for creating a quality training set for MLPs [29].

While AIMD simulations provide reliable data, they are limited in covering the diverse atomic configurations and thermodynamic ensembles of the potential energy surfaces [29]. In contrast, simple random sampling probes a wide range of configurations but overlooks local minima with unphysical over-weighting on high-energy configurations [29]. The RAG method overcomes these limitations by utilizing the advantages of random sampling and structural optimization from both approaches.

The RAG method generates the initial structures from randomized lattice structures, species arrangements, and atomic displacements. These initial structures from the RAG sampling are then optimized through 10~15 iterative steps of force minimization by DFT calculations, resulting in a training set that encompasses a wide spectrum of potential energy states. The resultant RAG dataset covers a broad potential surface, including local minima, which are likely to be missed by AIMD or simple random sampling. Since the RAG scheme constructs efficiently a diverse and comprehensive training set for MLPs, it is particularly useful for complex systems such as liquids, amorphous solids, and defective crystals with less computational loads than AIMD construction.

The GST225 RAG dataset comprised 66457 atomic configurations, covering a broad range of structural phases (liquid, amorphous solid, metastable cubic, and hexagonal) with potential energies ranging $-4.2 \sim -3$ eV/atom (see Supplemental Material for further information on the RAG dataset and its potential energy plot [28]). Approximately 5% (3457 configurations) of the RAG dataset was randomly selected to form the validation set, and the remaining $\sim 95\%$ (63000 configurations) constituted the training set.

Our RAG training dataset encompasses an extensive array of configurations, including single elements (Ge, Sb, Te), binaries (GeTe, Sb₂Te₃), and ternaries, along with a variety of segregated structures, covering a diverse range of stoichiometries and structures. This breadth is validated through t-SNE analysis [29], which visualizes data distribution by reducing non-primal dimensionalities using the similarity check [31]. Extrapolation capability of MLPs across various stoichiometries was also demonstrated in a recent study of GST compounds [32].

C. Linear chain of p -bonding

We employed the linear chain of p -bonding (p -bonding chain) model to analyze the structure of c-GST [14]. From a stoichiometric perspective, the p -bonding network in GeTe is simple, with a formula unit of GeTe possessing six valence p -electrons and their p_x -, p_y -, and p_z -orbitals tending to align in a linear chain-like structure. In contrast, Sb₂Te₃ features a vdW-gapped structure with successive stacking of quintuple layers, containing 18 p -electrons in a formula unit. This stoichiometric interpretation applies to various chemical compositions

of the pseudo-binary compounds (GeTe) _{m} -(Sb₂Te₃) _{n} .

The p -bonding chain of c-GST in this study was defined as the sequential bonding of cations and anions with restricted bonding connections that are less than 4 Å in length and larger than 135° in dihedral angle. The first peak of the radial distribution function (RDF) of c-GST at 700 K terminates at 4 Å (see Supplemental Material for the RDF and ADF of c-GST at 700 K [28]). Every linear p -bonding chain in c-GST is truncated by two vacancies, and its length is measured by the number of p -bonding units or equivalently by subtracting one from the number of constituent atoms. Notably, the structural network of p -bonding chains is fully determined by vacancy distribution, and thus its distribution can serve as a gauge of the vacancy ordering.

D. Vibrational density of states (VDOS)

The dynamical state of a simple harmonic oscillator can exhibit autocorrelation. Even when the dynamical phase of an oscillator stochastically collapses due to its finite lifetime, autocorrelation can still be picked for a large ensemble. The density of the vibrational states of the oscillators can be calculated by Fourier transforming the velocity autocorrelation functions,

$$g(\omega) = \frac{1}{N} \sum_j \int_{-\infty}^{\infty} dt e^{i\omega t} \gamma_j(t), \quad (1)$$

$$\gamma_j(t) = \frac{\langle \mathbf{v}_j(t+\tau) \cdot \mathbf{v}_j(\tau) \rangle_{\tau}}{\langle |\mathbf{v}_j(\tau)|^2 \rangle_{\tau}}, \quad (2)$$

where $g(\omega)$ is the vibrational density of states (VDOS) for N atoms, $\gamma_j(t)$ the atomic velocity autocorrelation function (VACF), $v_j(t)$ the velocity vector of atom j , and $\langle f(\tau) \rangle_{\tau}$ represents the ensemble average over τ [33, 34]. A long (>10 ps) and large (>1000 atoms) simulation is necessary to obtain a reliably converged VDOS. The frequency shift and linewidth broadening of phonons caused by their anharmonicity can be effectively captured by classical MD simulations. This method provides a reliable distribution of vibrational modes at temperatures above the Debye temperature T_D , as guaranteed by the energy equipartition theorem [33]. We note that the VACF captures not only phonons but also localized atomic vibration modes.

The VDOS of typical crystalline solids is proportional to ω^2 at low frequencies according to the Debye model. The reduced VDOS, $g(\omega)/\omega^2$, is used to investigate the low-frequency dynamics that determines the thermal transport properties. For perfect crystals, no peaks appear in the reduced VDOS below the frequency of a Brillouin peak, which originates from Van Hove singularity by the transverse acoustic (TA) phonons near the Brillouin zone boundaries [35]. In contrast to the Brillouin peaks, there may exist another kind of peak in the VDOS spectrum below the Brillouin peaks in amorphous solids. These peaks are called boson peaks and are

known to originate from structural disorder [35, 36], low mechanical rigidity [37], or low atomic density [38].

E. DFT calculations

The potential energies and forces of the RAG configurations were calculated using the Vienna *Ab initio* Simulation Package (VASP) with the projector augmented-wave (PAW) method [39, 40]. The Perdew-Burke-Ernzerhof functional was adopted for the exchange-correlation term [41], and the DFT-D3 method with Becke-Johnson damping function was used to account for additional van der Waals energy correction [42, 43]. The cutoff energy for the plane-wave basis set was set to 520 eV, and momentum space sampling was performed with an isotropic spacing of 0.13 \AA^{-1} . We note that structural parameters can be affected by the choice of pseudopotentials [44–46]. In particular, it has a long history that electronic and structural properties are sensitive to the way that semicore *d* orbitals are treated in pseudizing as valence or core states. Also, the type of exchange-correlation functional and treatment of long-range dispersion interaction may affect the total energy and the forces, and resultingly the training data set [23, 47]. Thus, care must be taken to construct the training data set that represent structural features properly. Otherwise, unphysical consequences such as wrong bonds, under- or over-estimation of structural orders may result in. The atomic configurations were visualized using the Atomic Simulation Environment (ASE) package [48].

III. RESULTS

A. Vacancy ordering during annealing

The annealing of c-GST was simulated to investigate the rearrangement of cations and vacancies. The initial atomic configuration in the annealing simulation was randomly generated by RAG (Fig. 1a). Our GST225

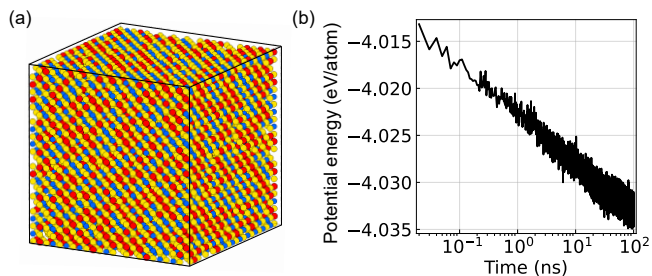


FIG. 1. (a) The initial RAG configuration of c-GST and (b) the potential energy change during the annealing at 700 K. The balls in blue, red, and yellow in (a) correspond to Ge, Sb, and Te atoms, respectively.

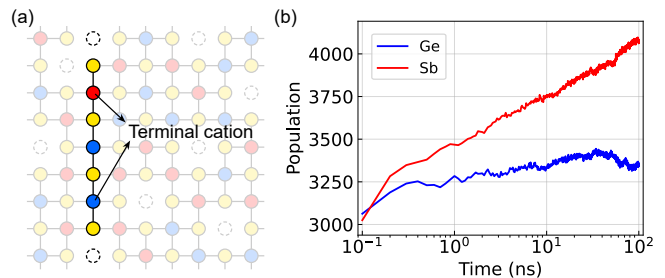


FIG. 2. (a) Schematic illustration of the terminal cation and (b) changes in terminal-cation-site population. In (a), colored circles represent atoms and dashed circles denote vacancies. The set of highlighted atoms in (a) comprises the *p*-bonding chain of length 6 truncated by two vacancies. The population in (b) refers to the number of atoms occupying the terminal-cation sites (Ge: blue, Sb: red) as a function of the annealing time on a logarithmic scale (all time points are shifted by 100 ps).

potentials reproduced successfully the c-GST structure through direct crystallization simulation from a melt-quenched amorphous structure. The resulting structure was polycrystalline, exhibiting many domain walls. To focus on the vacancy ordering analysis, we chose the RAG-generated structure as an initial configuration for the c-GST annealing simulation. We verified that the RAG configuration contains local structures similar to the directly crystallized configuration and that the main conclusion in our simulations is not affected by the choice of initial c-GST configurations (see Supplemental Material for the crystallization of melt-quenched a-GST, the comparison of the c-GST structures constructed by RAG and direct crystallization simulation, and the structure and VDOS of c-GST directly crystallized from a-GST [28]). The initial RAG configuration was the $12 \times 12 \times 12$ supercell of the rock-salt FCC conventional cell, with 13824 lattice points in total. All 6912 anion sublattices were occupied by Te atoms, while the remaining 6912 cation sublattices were occupied by 2765 Ge, 2765 Sb, and 1382 vacancies at random. The cubic box was $\sim 72.17 \text{ \AA}$ in size and had a mass density consistent with the experimentally measured value of c-GST $\sim 6.27 \text{ g/cm}^3$, or equivalently $\sim 0.0331 \text{ atom/\AA}^3$ [49]. The annealing simulation was carried out using the isothermal-isochoric (NVT) ensemble at 700 K, at which the crystal growth rate is reported to be the highest [9]. After a 100 ns annealing simulation, the c-GST system was transformed into a vacancy semi-ordered cubic state with the potential energy lowered by 20 meV/atom (Fig. 1b).

The changes in atomic structures were not noticed from RDF and ADF comparison (see Supplemental Material for the comparison of partial RDFs and total ADFs of c-GST annealed for 10 ps and 100 ns [28]). In order to investigate the structural changes caused by annealing, we monitored the population of cations at the terminal-cation sites of the *p*-bonding chains (Fig. 2).

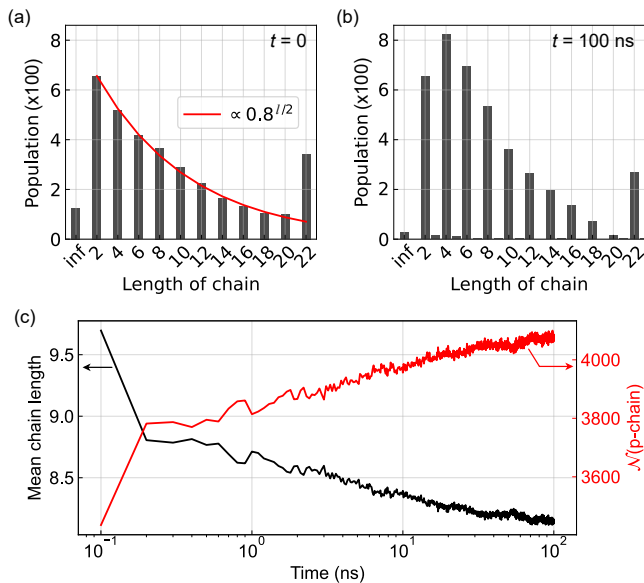


FIG. 3. The p -bonding chain length histogram at (a) $t=0$ and (b) 100 ns. The x -tick label “inf” indicates an infinitely long p -bonding chain due to the open boundary condition, i.e., a p -bonding chain of length 24 with the chain ends interconnected over the cell. The fitting curve in red in (a) is $\sim 0.8^{l/2}$ with l as the chain length. The sum of all p -bonding chain lengths remains almost constant in the range of 33100~33300. (c) The change in the mean p -bonding chain length (black curve) and the number of p -bonding chains (red curve).

The terminal-cation sites were occupied by Ge and Sb atoms at the same rate in the initial RAG configuration, but Sb atoms gradually outnumbered Ge atoms by annealing (Fig. 2b). After 100 ns of annealing, the number of Ge and Sb atoms occupying the terminal-cation sites were 3357 and 4073, respectively, which is an excess population of Sb by $\sim 21\%$. The formation of Sb-Te-vacancy configurations is a key structural change toward the hexagonal Kooi phase, in which p -bonding chains always have Sb atoms at their terminal-cation sites. As the vacancies became ordered, the number of p -bonding chains increased, as did the population of Ge and Sb atoms at terminal-cation sites (Fig. 2b and Fig. 3c). We point out that a p -bonding chain of length 2 has only one terminal-cation site.

The change in the number and length distribution of the p -bonding chains during annealing was investigated (Fig. 3). In an infinitely large virtual c-GST with randomly distributed cations and vacancies, the length distribution of the p -bonding chains converges to $P(l) = x(1-x)^{l/2}$, where x is the ratio of vacancies to cation sites, and l is the length of the p -bonding chain. For cubic GST225, $x=0.2$ and the distribution of p -bonding chain lengths follows the power law $P(l) \propto 0.8^{l/2}$. The initial RAG configuration of a finite size with periodic boundary conditions shows a good fit to the power law distribution of p -bonding

chain lengths (Fig. 3a). After annealing, the number of p -bonding chains with lengths >16 decreased, while the number of the p -bonding chains with lengths 4~14 increased (Fig. 3b). The total number of the p -bonding chains increased while the average length of the p -bonding chains decreased to 8.14 by annealing (Fig. 3c). The vacancy-ordered configurations in the VOC and hexagonal Kooi phases of GST225 consist only of p -bonding chains of length 8.

We defined the position of vacancies to investigate their distribution and migration. Since vacancies in c-GST are not naturally identified, we defined their positions through the following steps. First, we created an excessive number of vacancy candidates at the 3 Å-prolonged positions along all the p -bonding chains. These candidates were then grouped into thousands of sets, following the rule that two vacancy candidates belong to the same set if their inter-vacancy-candidate distance is less than 2.2 Å. By regarding the candidates within a set as duplicates of the genuine vacancy, we determined the vacancy position as the mean position of all candidates within the set. Faulty vacancies that had any neighboring atoms closer than 2 Å were removed. We note that defining a vacancy and its position in practical c-GST structures, especially at elevated temperatures, becomes ambiguous. Despite the number of vacancies in the ideal c-GST structure being 1382, lattice distortions and atomic migrations in the actual annealing simulation at 700 K resulted in fewer vacancies: 1382, 1252, 1315, 1363, and 1373 vacancies were found at $t=0$ s, 10 ps, 100 ps, 1 ns, 10 ns, and 100 ns, respectively. See Supplemental Material for an example of the vacancy structure of c-GST [28].

The vacancy distribution was investigated using RDF and ADF (angular distribution function) of vacancies (Fig. 4). The cutoff distance for the vacancy ADF calculation was 5.2 Å, which encompasses the first peak of the vacancy RDF. In the initial RAG configuration without any atomic displacement from the ideal c-GST lattice points, the sharp peaks were observed in the vacancy RDF at $\sim 3\sqrt{2}$ Å, 6 Å, $3\sqrt{6}$ Å, and $6\sqrt{2}$ Å, and in the vacancy ADF at $\sim 60^\circ$, 90° , 120° , and 180° (Fig. 4a). Among the vacancy-RDF and ADF peaks, the 6 Å and 90° peaks cannot exist in the vacancy fully ordered configurations of the VOC and hexagonal phases. Throughout the annealing process, the intensities of the 6 Å and 90° peaks were gradually reduced by the rearrangement of vacancies (Fig. 4). This reduction in the intensities of these two peaks is evidence of local vacancy ordering in the layers along the (111) direction.

To analyze the increase in the vacancy-RDF first peak intensity at $3\sqrt{2}$ Å and the reduction of the vacancy-RDF second peak intensity at 6 Å in a more specific way, the peak areas were calculated. The mean coordination number of vacancy-vacancy (V-V) duos can be calculated by integrating the vacancy-RDF first peak (Fig. 4) ranging from 3.5 Å to 5.2 Å, weighted by the area of a sphere $4\pi r^2$ times the vacancy number density ~ 0.00368

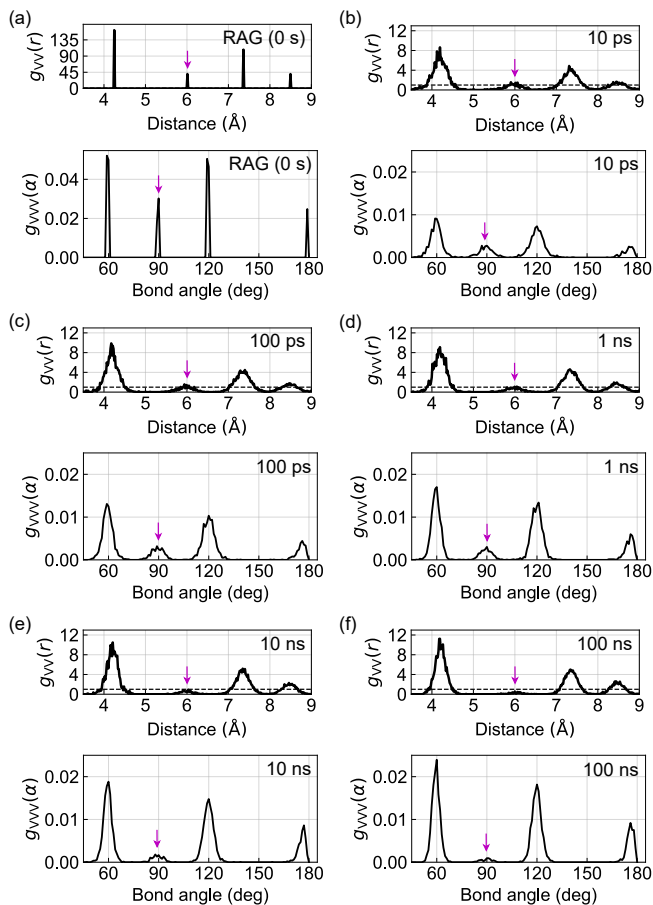


FIG. 4. Vacancy radial distribution function (g_{VV}) and vacancy angular distribution function (g_{VVV}) for (a) 0 s, (b) 10 ps, (c) 100 ps, (d) 1 ns, (e) 10 ns, and (f) 100 ns configurations, respectively. The purple arrows indicate the peaks that should disappear in the vacancy fully ordered configurations.

\AA^3 (Fig. 5a). A vacancy located at a cation lattice site in *c*-GST has 12 first nearest cation sites at a distance of $3\sqrt{2}$ Å. The expectation number of the V-V duos is 2.4 for the vacancy-disordered configurations, while it is 6 for the vacancy fully ordered configurations. The coordination number of V-V duos gradually increased from 2.44 to 2.70 by annealing (Fig. 5a).

The vacancy-RDF second peak at 6 Å originates from the straight vacancy-Te-vacancy (V-Te-V) trio illustrated in the inset of Fig. 5b. The number of V-Te-V trios is calculated by integrating the vacancy-RDF second peak (Fig. 5b) ranging from 5.3 Å to 6.6 Å. Since a vacancy has 6 first-nearest Te atoms at a distance of 3 Å, the average coordination number of V-Te-V trios converges to 1.2 for randomly disordered vacancies. The coordination number of the trios decreased monotonically from 1.2 to 0.2 during the 100 ns annealing process (Fig. 5b).

The increase in the V-V duo coordination by $\sim 11\%$ and the reduction of V-Te-V trio coordination by $\sim 83\%$ serve

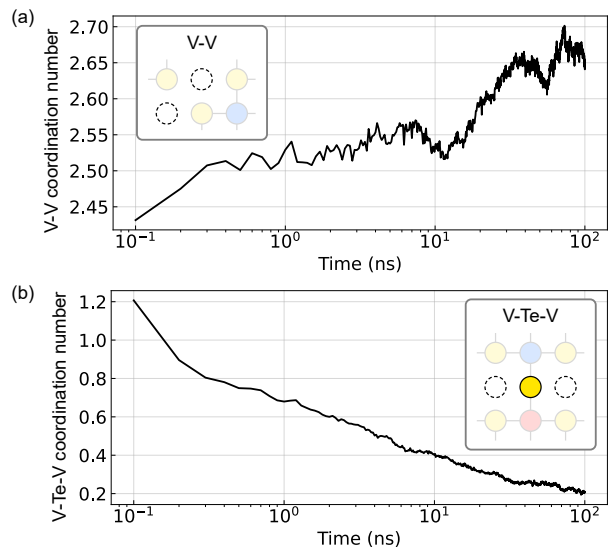


FIG. 5. Change in the number of (a) V-V duos and (b) straight V-Te-V trios during annealing. The insets illustrate example of the V-V duo and V-Te-V trio configurations. The annealing time is given on a logarithmic scale shifted by 100 ps.

as evidence of vacancy ordering towards planar vacancy layers. For example, when a Te atom neighbors one vacancy in a direction (e.g., *x*-axis), the Te atom tends to simultaneously neighbor other vacancies in the other directions (e.g., *y* and *z*-axis). On the other hand, a situation in which a Te atom neighbors two vacancies in a single direction on both sides is extremely unfavorable.

Migration of a vacancy is equivalent to the positional exchange of a vacancy with a neighboring cation. To determine whether Ge or Sb is more responsible for vacancy migration, we calculated the mean squared displacement (MSD) from the initial RAG configuration during annealing. See Supplemental Material for the species-wise MSD along the annealing [28]. During the first 1 ns, the MSD of Sb atoms increased more rapidly and became larger than the MSD of Ge by 0.5 \AA^2 . The MSD gap between Ge and Sb remained $\sim 0.5 \text{ \AA}^2$ after 1 ns, indicating that Ge and Sb atoms equally contributed to vacancy migration. Despite having a smaller covalent radius (1.21 Å) and lighter mass (72.64 a.u.) than Sb (covalent radius of 1.40 Å and mass of 121.76 a.u.), Ge did not contribute more to vacancy migration than Sb.

B. Debye-Waller thermal *B* factor

The Debye-Waller thermal isotopic factor $B_{\text{iso}} = \frac{8\pi^2}{3} \langle u^2 \rangle$ was calculated at five time points (10 ps, 100 ps, 1 ns, 10 ns, and 100 ns), where $\langle u^2 \rangle$ is the mean squared displacement of ions (Fig. 6). We obtained B_{iso} at each time point with a 100 ps-long,

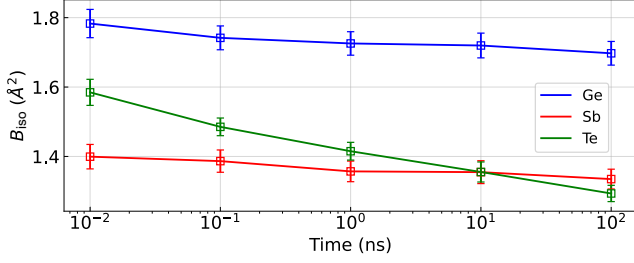


FIG. 6. Change in $B_{\text{iso}}(T=300 \text{ K})$ by annealing. The error bars indicate the standard deviation of the thermal factors calculated from equilibrium MD simulations.

300 K, NVT-MD simulation followed by a 50 ps-long thermal equilibration. The mean thermal factors of Ge, Sb, and Te decreased monotonically until 100 ns. Notably, the mean thermal factor of Te atoms $B_{\text{iso}}^{\text{Te}}$ decreased significantly by $\sim 19\%$ (from $B_{\text{iso}}^{\text{Te}}=1.58 \text{ \AA}^2$ at 10 ps to $B_{\text{iso}}^{\text{Te}}=1.29 \text{ \AA}^2$ at 100 ns). The vacancy disorder in the initial RAG configuration seem responsible for the abnormally large thermal factor of Te atoms. The thermal factors of c-GST measured by neutron and X-ray diffraction at room temperature were $B_{\text{iso}}^{\text{Ge}}=1.63 \text{ \AA}^2$, $B_{\text{iso}}^{\text{Sb}}=1.64 \text{ \AA}^2$, and $B_{\text{iso}}^{\text{Te}}=1.671 \text{ \AA}^2$ [50]. The mean thermal factor $B_{\text{iso}}\sim 1.58 \text{ \AA}^2$ of the configuration annealed for 10 ps is close to the measurement.

The sensitivity of $B_{\text{iso}}^{\text{Te}}$ to annealing suggests that the vacancy distribution significantly affects the dynamics of Te lattices. This result is convincing from our finding that vacancies are always surrounded by the nearby Te atoms. It also implies that the thermal B factor of Te atoms could potentially serve as an indicator of the degree of vacancy ordering.

C. Boson peak

We calculated the VDOS of c-GST to analyze its dynamic states through vacancy ordering (Fig. 7). The VDOSs were calculated from the VACF of the same 300 K NVT-MD simulations used to calculate the thermal factors. The change in the overall shape of the VDOS is negligible, except for the localized vibration modes at $\sim 0.575 \text{ THz}$. These localized modes are more clearly recognized in the reduced VDOS as scaled by ω^{-2} (Fig. 7b), forming a so-called boson peak. The VDOS of the configurations at 10 ps, 100 ps, and 1 ns show distinctive boson peaks, while those at 10 ns and 100 ns do not. Notably, the boson peak modes involve with the vibration of Te atoms. Another peak at $\sim 1.1 \text{ THz}$ (Fig. 7b) is the Van Hove singularity developed by the TA phonon modes at the zone boundaries, namely the Brillouin peak. We found that this Brillouin peak is evenly contributed by all elements, indicating the delocalized feature of the phonon modes. A slight shift in the position of the Brillouin peak is an artifact due

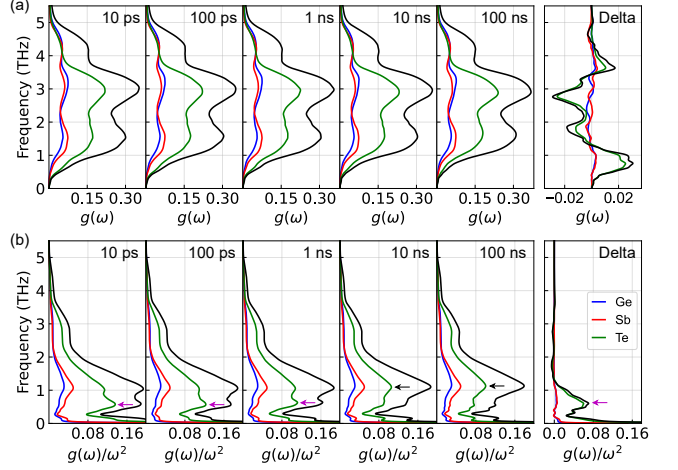


FIG. 7. Partial VDOS of c-GST thermally annealed for 10 ps, 100 ps, 1 ns, 10 ns, and 100 ns. The reduced VDOS in (b) is scaled by ω^{-2} from the VDOS in (a). The rightmost panel labeled “Delta” shows the subtraction of VDOS at 10 ps by that at 100 ns. The arrows in purple highlight the distinct boson peaks and those in black the Brillouin peaks. All curves are smeared by Gaussians with a 0.05 THz width.

to the tail of the nearby boson peak. The shape of the Brillouin peak does not change as the vacancies become ordered.

The normal mode analysis for the boson peak vibrational modes showed that the boson peak consists primarily of the vibrational modes localized at Te atoms (See Supplemental Material for visualization of the atom-wise boson peak intensity [28]). The boson peak intensity projected on atom j provides a strong signature of the correlation between the vacancy distribution and the boson peak. We calculated the atom-projected boson peak intensity $g_j(\omega_{\text{BP}})/\omega_{\text{BP}}^2$ from the atom-projected VDOS $g_j(\omega) = \frac{1}{3N} \sum_i \delta(\omega - \omega_i) \sum_\alpha u_{i,j,\alpha}^2$, where u_i is the polarization vector of the i -th vibrational normal mode, N the total number of atoms, and $\alpha = x, y, \text{ or } z$. We found that configuration-averaged value of the atom-projected boson peak intensity $g_j(\omega_{\text{BP}})/\omega_{\text{BP}}^2$ is proportional to the number of vacancies at the cation sites nearest to Te atom j (Fig. 8a). Moreover, the boson peak is contributed most by Te atoms that have a specific arrangement of neighboring vacancies. In Fig. 8b, we observe that the boson peak intensity is almost linear to the number of V-Te-V trios. This finding becomes more apparent when we compare the contribution to the boson peak from the modes localized at Te atoms with two neighboring vacancies. The contribution is large when a Te atom and two vacancies form a straight trio (V-Te-V) but, for V-V duos, it is almost the same as the case for 0 or 1 neighboring vacancy (Fig. 8c). We note that the V-V duo formation is the building block for the vacancy layers (i.e., vacancy ordering) as found in the hexagonal structure.

These findings support that the disappearance of the

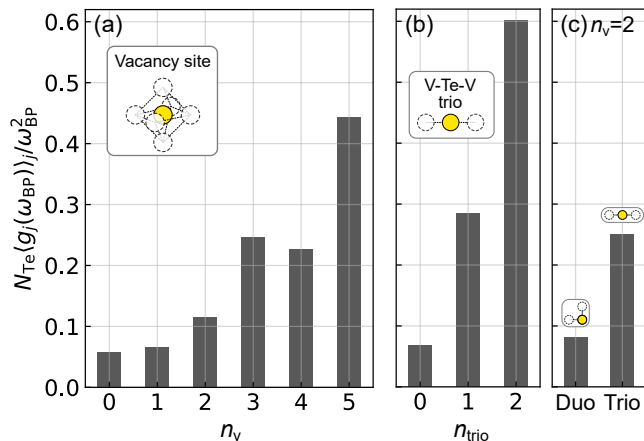


FIG. 8. Correlation between the vacancy distribution and boson peak intensity. Configuration-averaged boson peak intensity projected into a Te atom in terms of (a) the number of vacancies (n_v) at the cation sites nearest to Te, (b) the number of straight trios (n_{trio}), and (c) the two characteristic configurations (V-V duo and V-Te-V trio) of Te atoms with two neighboring vacancies ($n_v=2$). The boson peak intensity is scaled by the number of Te atoms N_{Te} (=6912) for comparison to the boson peak in Fig. 7.

boson peak is directly attributed to the vacancy ordering and, in other words, that the structural disorder in c-GST contributes to the development of the boson peak. The boson peak intensity in c-GST appears to be highly correlated with the large thermal factor of Te atoms. A strong correlation between boson peak modes and thermal factors was previously observed in a two-dimensional power-law potential model [36].

IV. DISCUSSION

We constructed a machine-learned GST225 potential using the RAG dataset and simulated 100 ns annealing of c-GST at 700 K. After annealing, the initial RAG configuration of c-GST with vacancy disorder transformed into a vacancy semi-ordered cubic structure with a lowered energy by ~ 20 meV/atom. The structural transition was captured by the p -bonding chain model and the vacancy distribution analysis. In the final vacancy semi-ordered configuration, Sb atoms occupied the terminal-cation sites in the p -bonding chains 21% more frequently than Ge atoms. The number of p -bonding chains longer than 16 decreased by annealing, while the number of shorter p -bonding chains increased. The change in vacancy distribution also supports vacancy ordering. Vacancies tend to be located next to Te atoms already neighboring other vacancies, while the configuration of

a straight V-Te-V trio is extremely unfavored. Our annealing simulation of 100 ns may not be long enough to achieve vacancy ordering on a full scale, but all observed structural features consistently indicate the progression of layer-like vacancy ordering.

We identified several key features accompanying the vacancy ordering. A boson peak develops at ~ 0.575 THz due to the vacancy disorder at the initial stages of annealing ($t < 1$ ns) and then gradually disappears as vacancies are ordered. This formation and evolution of the boson peak by the vacancy ordering is in sheer contrast to the common observation that the boson peaks are formed in amorphous materials. The abnormal boson peak in c-GST is attributed to the modes at Te atoms with certain but energetically unfavorable configurations, while the lattice structure retains the cubic symmetry. We note that such a dynamical phase transition without a change in the density or symmetry of the lattice structure is a unique feature of c-GST. The Debye-Waller thermal B factor of Te decreased by $\sim 19\%$ in the vacancy semi-ordered cubic phase, indicating its correlation with the boson-peak suppression. The observable response of the thermal factor and the boson peak suggests that they can serve as dynamic indicators of the vacancy ordering. Controlling the localized boson peak modes by the vacancy ordering can be an efficient tool for manipulating the thermoelectric properties of the chalcogenides. Our findings by large-scale MLMD simulations provide a microscopic understanding of the vacancy ordering, which can be utilized for developing multilevel memories and neuromorphic devices using phase-change materials.

DATA AVAILABILITY

The RAG-dataset-trained $\text{Ge}_2\text{Sb}_2\text{Te}_5$ potential in LAMMPS pair-potential format, the RAG configuration dataset and other data supporting the findings of this study and the computational tools (simulation script and analysis codes) used in this study are available from the corresponding author upon reasonable request.

ACKNOWLEDGMENTS

This study was supported by the National Research Foundation of Korea (NRF) Grant No. 2022R1A2C1006530 funded by the Korea government (MSIT), and by Samsung Electronics Co., Ltd (Grant number IO201214-08146-01). Supercomputing resources including technical support was provided by Supercomputing Center, Korea Institute of Science and Technology Information (Contract No. KSC-2022-CRE-0366).

[1] M. Wuttig and N. Yamada, *Nature Materials* **6**, 824 (2007).

[2] S. Raoux and M. Wuttig, *Phase Change Materials*, 1st ed. (Springer, New York, 2009).

- [3] G. W. Burr, M. J. Breitwisch, M. Franceschini, D. Garetto, K. Gopalakrishnan, B. Jackson, B. Kurdi, C. Lam, L. A. Lastras, A. Padilla, B. Rajendran, S. Raoux, and R. S. Shenoy, *Journal of Vacuum Science & Technology B* **28**, 223 (2010).
- [4] T. Siegrist, P. Jost, H. Volker, M. Woda, P. Merkelbach, C. Schlockermann, and M. Wuttig, *Nature Materials* **10**, 202 (2011).
- [5] N. Yamada and T. Matsunaga, *Journal of Applied Physics* **88**, 7020 (2000).
- [6] B. J. Kooi and J. T. M. De Hosson, *Journal of Applied Physics* **92**, 3584 (2002).
- [7] A. V. Kolobov, P. Fons, A. I. Frenkel, A. L. Ankudinov, J. Tominaga, and T. Uruga, *Nature Materials* **3**, 703 (2004).
- [8] J. Hegedüs and S. R. Elliott, *Nature Materials* **7**, 399 (2008).
- [9] J. Orava, A. L. Greer, B. Gholipour, D. W. Hewak, and C. E. Smith, *Nature Materials* **11**, 279 (2012).
- [10] R. Jeyasingh, S. W. Fong, J. Lee, Z. Li, K.-W. Chang, D. Mantegazza, M. Asheghi, K. E. Goodson, and H. S. P. Wong, *Nano Letters* **14**, 3419 (2014).
- [11] T. H. Lee and S. R. Elliott, *Physical Review B* **84**, 094124 (2011).
- [12] T. H. Lee and S. R. Elliott, *Advanced Materials* **29**, 1700814 (2017).
- [13] K. Shportko, S. Kremers, M. Woda, D. Lencer, J. Robertson, and M. Wuttig, *Nature Materials* **7**, 653 (2008).
- [14] Y.-S. Song and S.-H. Jhi, *Journal of Physics: Condensed Matter* **32**, 175401 (2020).
- [15] Y.-S. Song, J. Kim, and S.-H. Jhi, *Physical Review Applied* **9**, 054044 (2018).
- [16] B. Zhang, X.-P. Wang, Z.-J. Shen, X.-B. Li, C.-S. Wang, Y.-J. Chen, J.-X. Li, J.-X. Zhang, Z. Zhang, S.-B. Zhang, and X.-D. Han, *Scientific Reports* **6**, 25453 (2016).
- [17] T. Matsunaga, N. Yamada, and Y. Kubota, *Acta Crystallographica Section B: Structural Science, Crystal Engineering and Materials* **60**, 685 (2004).
- [18] T. H. Lee and S. R. Elliott, *Physical Review Letters* **107**, 145702 (2011).
- [19] J. Kalikka, J. Akola, J. Larrucea, and R. O. Jones, *Physical Review B* **86**, 144113 (2012).
- [20] I. Ronneberger, W. Zhang, H. Eshet, and R. Mazzarello, *Advanced Functional Materials* **25**, 6407 (2015).
- [21] J. Kalikka, J. Akola, and R. O. Jones, *Physical Review B* **94**, 134105 (2016).
- [22] I. Ronneberger, W. Zhang, and R. Mazzarello, *MRS Communications* **8**, 1018 (2018).
- [23] F. C. Mocanu, K. Konstantinou, T. H. Lee, N. Bernstein, V. L. Deringer, G. Csányi, and S. R. Elliott, *The Journal of Physical Chemistry B* **122**, 8998 (2018).
- [24] K. Konstantinou, F. C. Mocanu, T.-H. Lee, and S. R. Elliott, *Nature Communications* **10**, 3065 (2019).
- [25] F. C. Mocanu, K. Konstantinou, and S. R. Elliott, *Journal of Physics D: Applied Physics* **53**, 244002 (2020).
- [26] Y.-X. Zhou, H.-Y. Zhang, V. L. Deringer, and W. Zhang, *physica status solidi (RRL) – Rapid Research Letters* **15**, 2000403 (2021).
- [27] S. Bätzner, A. Musaelian, L. Sun, M. Geiger, J. P. Mailoa, M. Kornbluth, N. Molinari, T. E. Smidt, and B. Kozinsky, *Nature Communications* **13**, 2453 (2022).
- [28] See Supplemental Material for the details of RAG dataset and its potential energy plot; the NequIP training parameters; the validation of the GST225 potential; the RDF and ADF of c-GST at 700 K; an example of the vacancy structure of c-GST; the RDF and ADF changes in annealing simulation; the species-wise mean squared displacement along the annealing; the longitudinal and transverse decomposition of VDOSs; the examples of the atom-wise intensity of the boson peak modes; the structure and VDOS of c-GST directly crystallized from a-GST; lattice thermal conductivity calculated by Müller-Plathe rNEMD simulation.
- [29] Y.-J. Choi and S.-H. Jhi, *The Journal of Physical Chemistry B* **124**, 8704 (2020).
- [30] N. Yamada, E. Ohno, K. Nishiuchi, N. Akahira, and M. Takao, *Journal of Applied Physics* **69**, 2849 (1991).
- [31] L. van der Maaten and G. Hinton, *Journal of Machine Learning Research* **9**, 2579 (2008).
- [32] Y. Zhou, W. Zhang, E. Ma, and V. L. Deringer, *Nature Electronics* **6**, 746 (2023).
- [33] J. M. Dickey and A. Paskin, *Physical Review* **188**, 1407 (1969).
- [34] M. T. Dove, *Introduction to Lattice Dynamics*, Cambridge Topics in Mineral Physics and Chemistry (Cambridge University Press, Cambridge, 1993).
- [35] S. Ciliberti, T. S. Grigera, V. Martin-Mayor, G. Parisi, and P. Verocchio, *The Journal of Chemical Physics* **119**, 8577 (2003).
- [36] Y.-C. Hu and H. Tanaka, *Nature Physics* **18**, 669 (2022).
- [37] N. Tomoshige, H. Mizuno, T. Mori, K. Kim, and N. Matubayasi, *Scientific Reports* **9**, 19514 (2019).
- [38] A. I. Chumakov, G. Monaco, A. Fontana, A. Bosak, R. P. Hermann, D. Bessas, B. Wehinger, W. A. Crichton, M. Krisch, R. Rüffer, G. Baldi, G. Carini Jr, G. Carini, G. D’Angelo, E. Gilioli, G. Tripodo, M. Zanatta, B. Winkler, V. Milman, K. Refson, M. T. Dove, N. Dubrovinskaya, L. Dubrovinsky, R. Keding, and Y. Z. Yue, *Physical Review Letters* **112**, 025502 (2014).
- [39] G. Kresse and J. Furthmüller, *Physical Review B* **54**, 11169 (1996).
- [40] G. Kresse and D. Joubert, *Physical Review B* **59**, 1758 (1999).
- [41] J. P. Perdew, K. Burke, and M. Ernzerhof, *Physical Review Letters* **77**, 3865 (1996).
- [42] S. Grimme, J. Antony, S. Ehrlich, and H. Krieg, *The Journal of Chemical Physics* **132**, 154104 (2010).
- [43] S. Grimme, S. Ehrlich, and L. Goerigk, *Journal of Computational Chemistry* **32**, 1456 (2011).
- [44] D. Campi, L. Paulatto, G. Fugallo, F. Mauri, and M. Bernasconi, *Physical Review B* **95**, 024311 (2017).
- [45] J. Tominaga, A. V. Kolobov, P. Fons, T. Nakano, and S. Murakami, *Advanced Materials Interfaces* **1**, 1300027 (2014).
- [46] G. Lee and S.-H. Jhi, *Physical Review B* **77**, 153201 (2008).
- [47] A. Bouzid, G. Ori, M. Boero, E. Lampin, and C. Massobrio, *Physical Review B* **96**, 224204 (2017).
- [48] A. Hjorth Larsen, J. Jørgen Mortensen, J. Blomqvist, I. E. Castelli, R. Christensen, M. Dulák, J. Friis, M. N. Groves, B. Hammer, C. Hargus, E. D. Hermes, P. C. Jennings, P. Bjerre Jensen, J. Kermode, J. R. Kitchin, E. Leonhard Kolsbjerg, J. Kubal, K. Kaasbjerg, S. Lysgaard, J. Bergmann Maronsson, T. Maxson, T. Olsen, L. Pastewka, A. Peterson, C. Rostgaard, J. Schiøtz, O. Schütt, M. Strange, K. S. Thygesen, T. Vegge, L. Vilhelmsen, M. Walter, Z. Zeng, and K. W. Jacobsen, *Journal of Physics: Condensed Matter* **29**,

273002 (2017).

- [49] W. K. Njoroge, H.-W. Wöltgens, and M. Wuttig, *Journal of Vacuum Science & Technology A* **20**, 230 (2002).
- [50] S.-i. Shamoto, K. Kodama, S. Iikubo, T. Taguchi, N. Yamada, and T. Proffen, *Japanese Journal of Applied*

Physics **45**, 8789 (2006).

Supplemental Material for: Study of vacancy ordering and the boson peak in metastable cubic Ge-Sb-Te using machine learning potentials

Young-Jae Choi, Minjae Ghim, and Seung-Hoon Jhi*

*Department of Physics, Pohang University of Science and Technology, Cheongam-ro 77,
Pohang 37673, Republic of Korea*

**e-mail: jhish@postech.ac.kr*

Table S1. RAG dataset composition of GST225 potential. The main data (64650 frames) are highlighted in yellow. The item “random_frac” is an input parameter for RAG scripts. The (A×B) format in the “Num. frames” column means A (the number of RAG random configurations) times B (the number of structure relaxation steps for each RAG random configuration). The “Energy and Force RMSE” columns denote the root-mean-squared errors of corresponding datasets. The last-row class “etc (RAG)” is for the remaining data including the single-element (Ge/Sb/Te) systems and some segregated structures for example.

Target	Backbone structure	Size	random_frac	Num. frames	Energy RMSE (meV/atom)	Force RMSE (meV/Å)
Hexagonal states (ground states)	Kooi supercell	81 atoms	0	100 copies	55.7	2.62
	Petrov supercell	81 atoms	0	100 copies	29.9	3.90
	Inverted Petrov supercell	81 atoms	0	100 copies	42.2	12.0
	Ferro-GeTe supercell	81 atoms	0	100 copies	36.5	9.66
	Inv.-Fer. supercell	81 atoms	0	100 copies	32.1	8.95
	Petrov-Fer. supercell	81 atoms	0	100 copies	30.0	10.3
Kooi phase (thermally excited states)	Kooi unit cell	9 atoms	0.02	200	55.5	7.18
			0.1	200	55.7	32.0
	Kooi supercell	144 atoms	0.02	177	55.4	5.00
			0.1	185	55.4	22.0
Matsunaga and VOC	Six hexagonal supercells	81 atoms	0.25	1350×10 =13500	42.3	43.9
Rock-salt cubic phase			0.3	1064×15 =15960	33.8	43.8
Amorphous solid	Rock-salt FCC supercell	57 atoms	0.7	1256×15 =18840	41.7	95.8
Liquid or more			0.8	1050×15 =15750	32.5	103
etc (RAG)	-	-	-	1045	501	139
Total	-	-	-	66,457	49.0	75.0

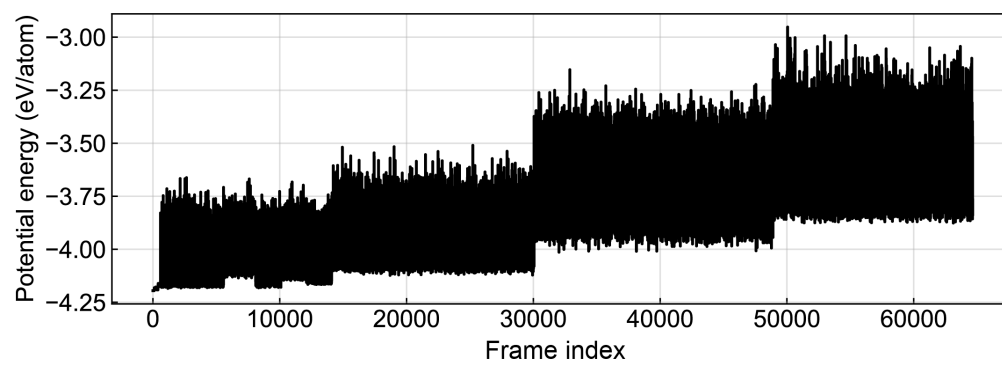


Fig. S1. The potential energy plot of the main RAG dataset. The composition of the main dataset is described in Table S1.

Table S2. NequIP training parameters used to produce GST225 potential.

NequIP version	0.5.3	learning_rate	2.e-3	
r_max	4.0	batch_size	5	
l_max	3	loss_coefs	forces	1.e+3
num_layers	5		total_energy	1
num_features	8		PerAtomMSELoss	
parity	false	optimizer_name	adam	
nonlinearity_type	gate	lr_scheduler_name	ReduceLROnPlateau	
num_basis	8	lr_scheduler_patience	1	
polynomialCutoff_p	6	lr_scheduler_factor	0.6	
invariant_layers	2	default_dtype	float32	
invariant_neurons	64	seed	123	
use_sc	true	dataset_seed	456	

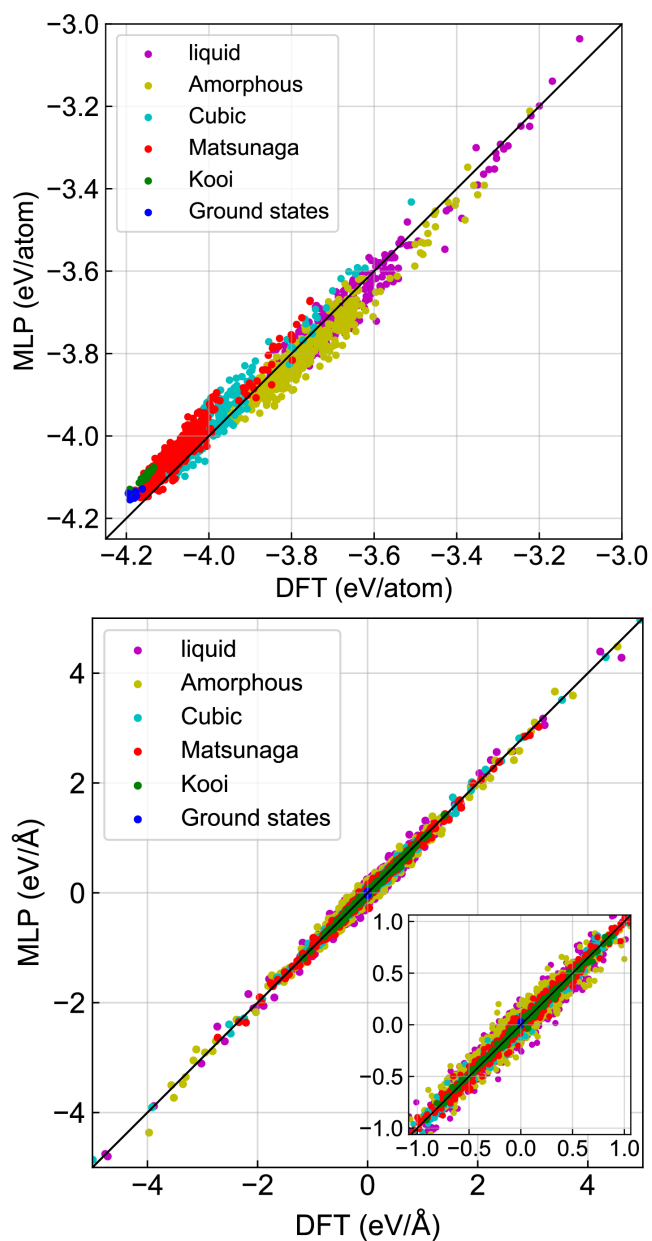


Fig. S2. Comparison of energy (upper panel) and force (lower panel) calculations between VASP (DFT) and NequIP (MLP).

Validation of GST225 potential

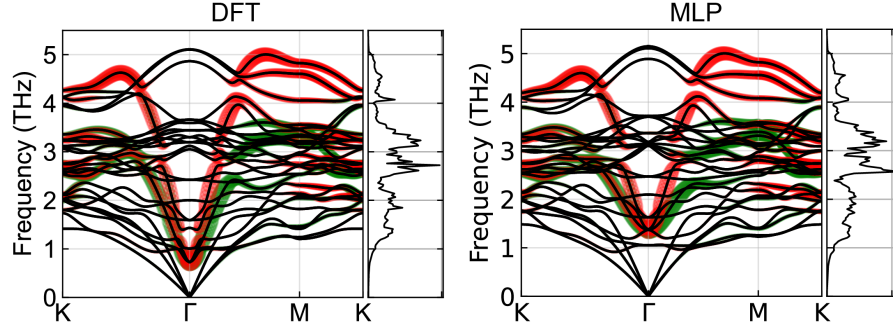


Fig. S3. Phonon band structure of Kooi phase calculated by VASP (DFT) and NequIP (MLP) potentials of GST225. Two narrow panels attached to the right side of phonon band plots are phonon density of states. The similarity of each mode to the E_u modes is expressed by green (E_u -A mode) and red (E_u -B mode) highlights. The thickness of highlights is proportional to the squared inner product of two modes $\sim |\boldsymbol{\epsilon} \cdot \boldsymbol{\epsilon}_{E_u-A,B}|^2$. E_u mode is a characteristic optical phonon mode of hexagonal GST, which is very sensitive to strain [1].

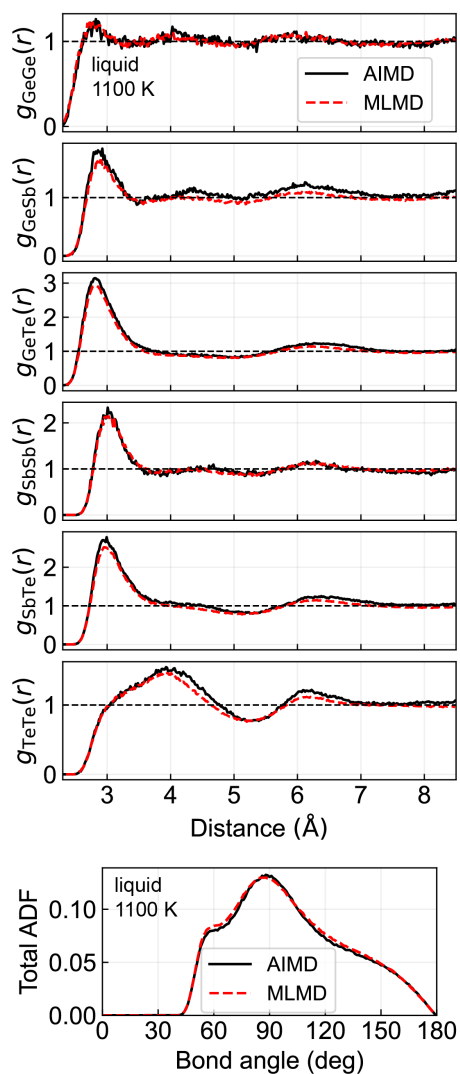


Fig. S4. Comparison of partial RDFs (top panel) and total ADFs (bottom panel) liquid GST225 at 1100 K. The AIMD simulation conditions: 54 atoms in a frame; NpT ($p=0$). The MLMD simulation conditions: 10368 atoms in a frame; NVT ensemble ($0.0309 \text{ atoms}/\text{\AA}^3$, the same density as the NpT ensemble).

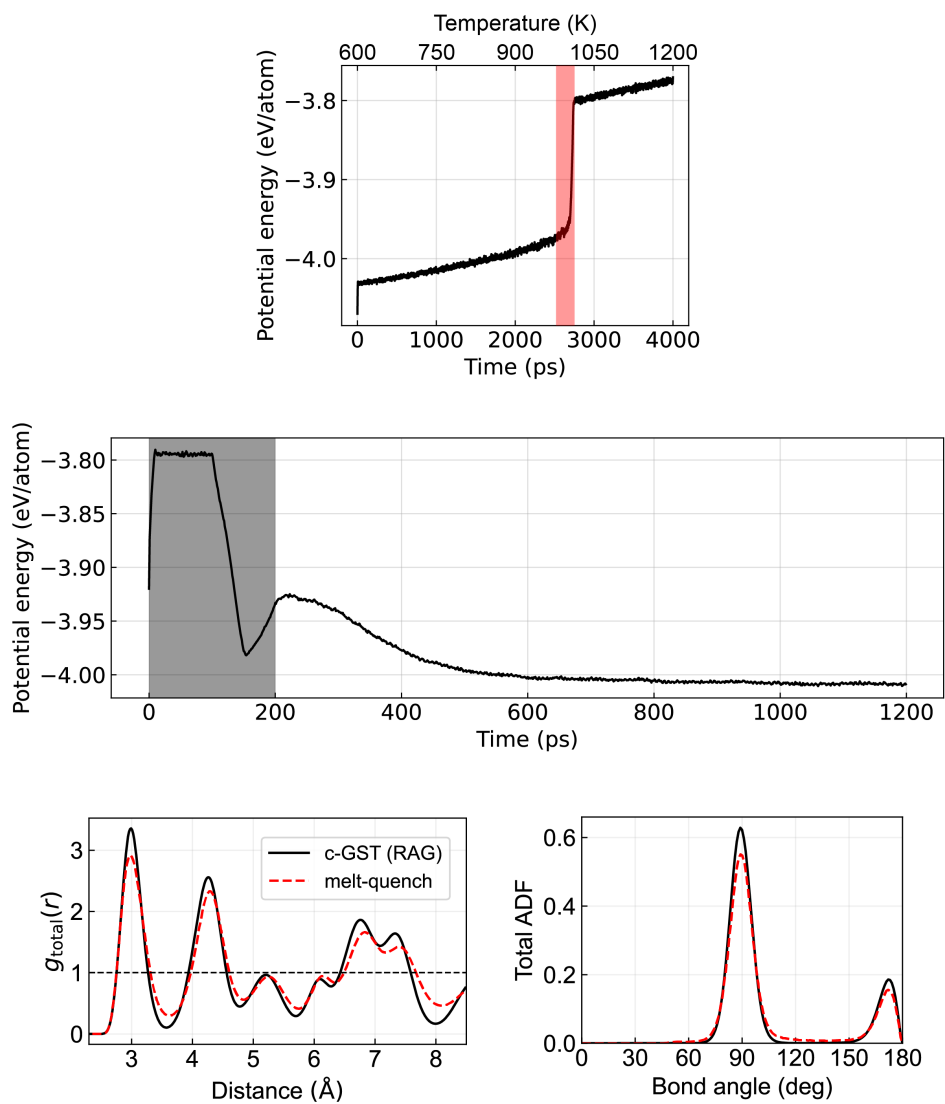


Fig. S5. Potential energy change of GST225 during melting (upper panel) and amorphous-to-cubic crystallization (middle panel). Bottom panel shows the comparison of RDFs and ADFs between the final structure of the crystallization (dashed line in red labeled melt-quench) and the c-GST structure from the annealing simulation discussed in the main manuscript (solid line in black labeled c-GST (RAG)). The heating rate in the melting simulation was 0.15 K/ps. In the upper panel, a red transparent box (975-1015 K) highlights the temperature range where the energy changes drastically. In the middle panel, a grey

transparent box (0-200 ps) marks the preparation step, which includes the melt-quenching and heating (melting at 1100 K for 0-100 ps, quenching to 300 K for 100-150 ps, and heating to 600 K for 150-200 ps).

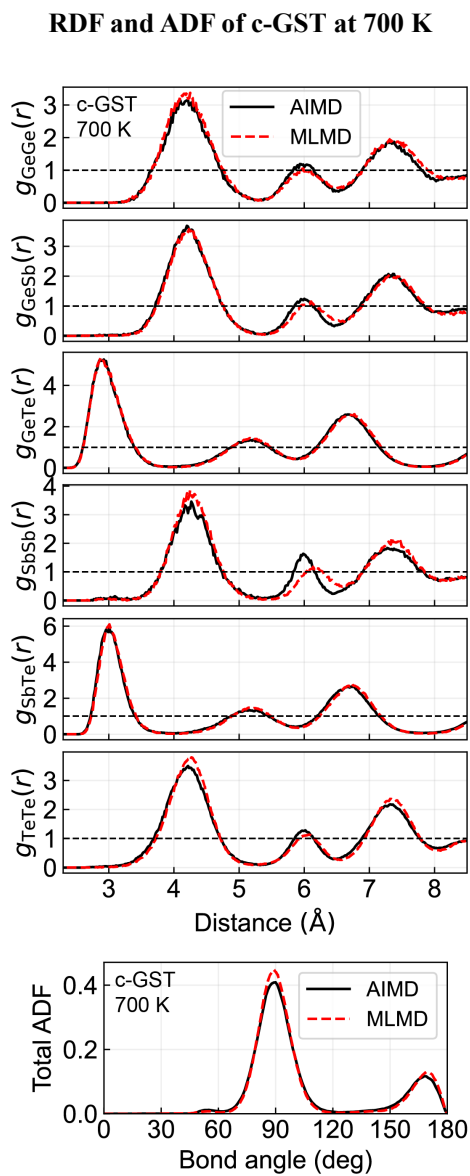


Fig S6. Partial RDFs (top panel) and total ADFs (bottom panel) of c-GST at 700 K. For MLMD plots, 10 intermediate atomic configurations between 0~100 ps of annealing simulation were used. The AIMD simulation conditions: 57 atoms in a frame; NVT (0.0331 atoms/Å³, the same density as the MLMD simulation).

An example of the vacancy configuration of c-GST

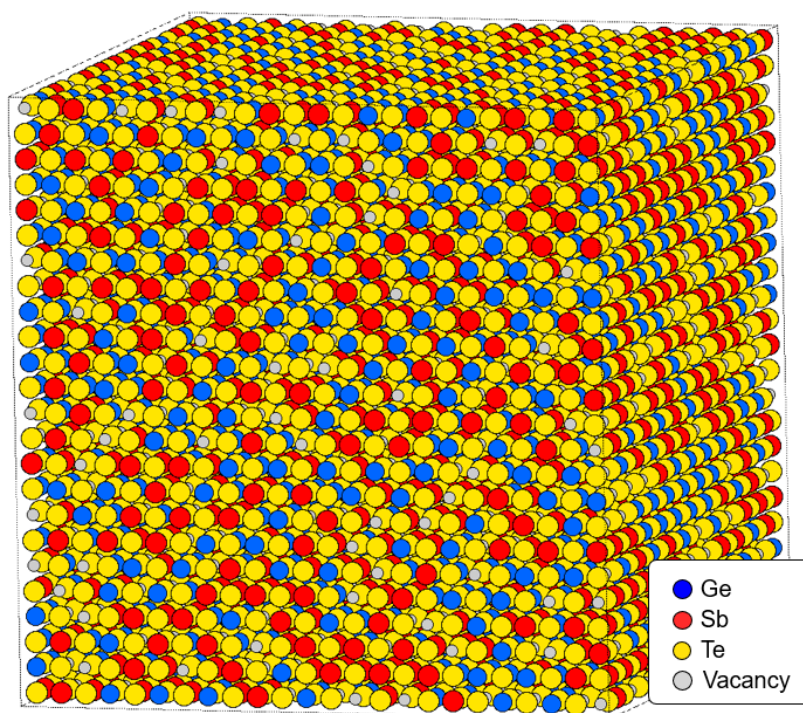


Fig. S7. The visualization of the initial RAG configuration including vacancies. The system contains 1382 vacancies (gray spheres) randomly arranged at cation sites. The algorithm used to find vacancies is described in the computational details section in the main manuscript.

RDF and ADF changes in annealing simulation

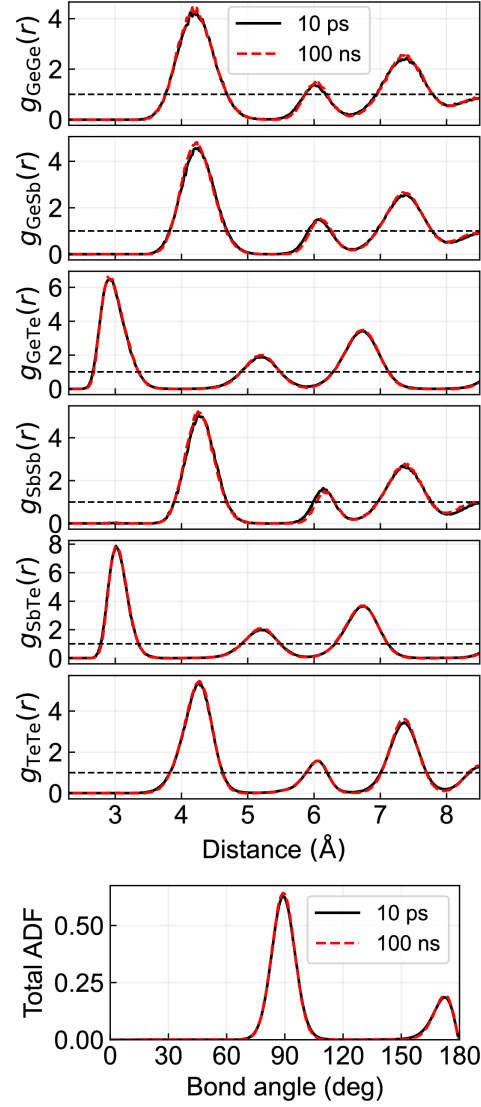


Fig. S8. Comparison of partial RDFs (top panel) and total ADFs (bottom panel) of c-GST annealed for 10 ps (solid line in black) and 100 ns (dashed line in red). To calculate RDFs and ADFs, the NVT (300 K) simulations were carried out the same way as for VDOS calculations in Fig. 7.

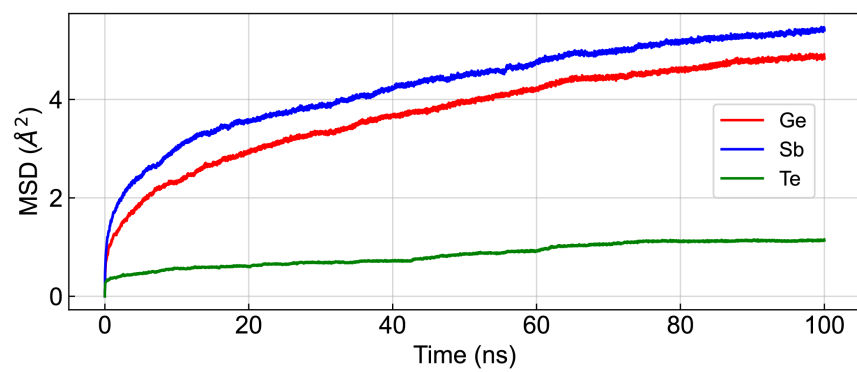


Fig. S9. Species-wise mean squared displacement along the annealing. The reference positions for the displacement measurement are the coordinates of the initial RAG configuration at 0 s of annealing.

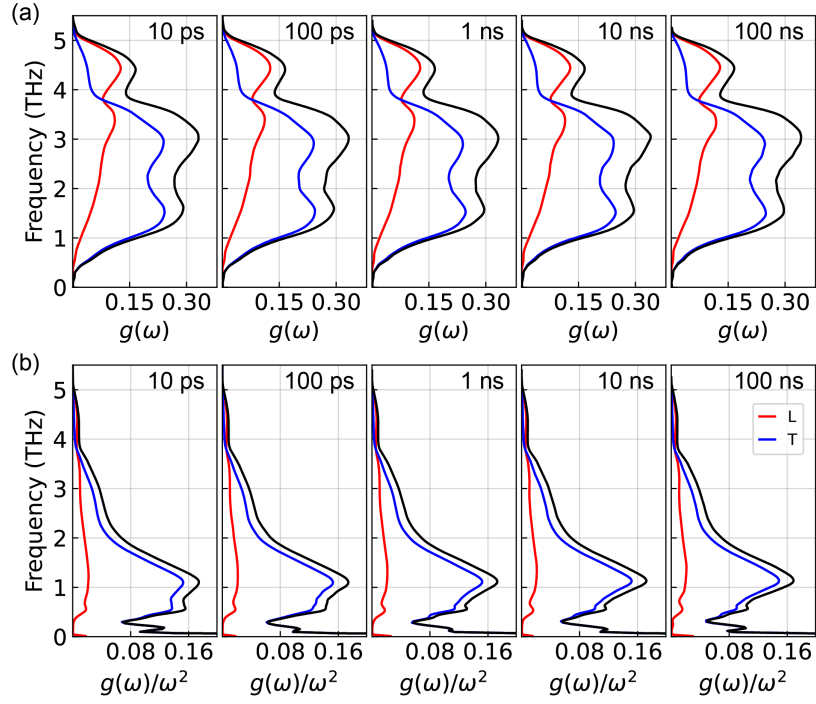


Fig. S10. Longitudinal-transverse decomposition of VDOSs based on the Voronoi cell method. Blue solid lines (labeled “T”) and red solid lines (labeled “L”) indicate the transverse and longitudinal modes, respectively. The decomposition into transverse and longitudinal mode is based on the Voronoi cell method introduced by Beltukov *et al.* [2].

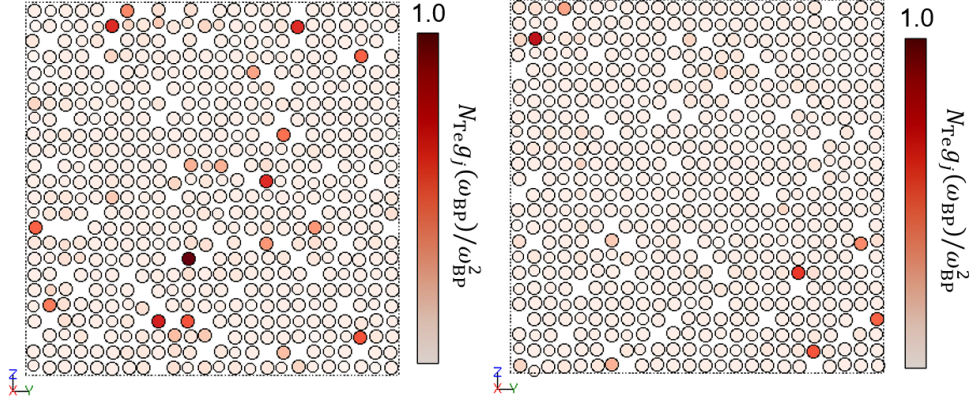


Fig. S11. Examples of the atom-wise intensity of the boson peak modes. The color of an atom indicates the atom-wise intensity of the vibrational modes with frequency 0.375~0.775 THz. The visualized 2-dimensional atomic configurations are the single-layer slices extracted from the 10 ps configuration of c-GST annealing.

Structure and VDOS of c-GST directly crystallized from a-GST

The RAG configuration was chosen as the initial structure for the annealing simulation instead of the c-GST configuration directly crystallized from a-GST since the latter has a more disordered Te lattice structure. The initial RAG configuration was found to be similar to the c-GST structure crystallized from a-GST, as demonstrated by the p -bonding chain length distribution and VDOS analyses (Fig. S12). The directly crystallized structure also displayed a power-law-like distribution of the p -bonding chain lengths, similar to the RAG configuration of Fig. 3a, but had a significant number of the odd-length p -bonding chains due to the distortion of the Te lattices. The VDOS of the directly crystallized structure at 300 K also showed a boson peak at ~ 0.560 THz, which was broadened by a 500 ps-long annealing process and the distortion of the Te lattices.

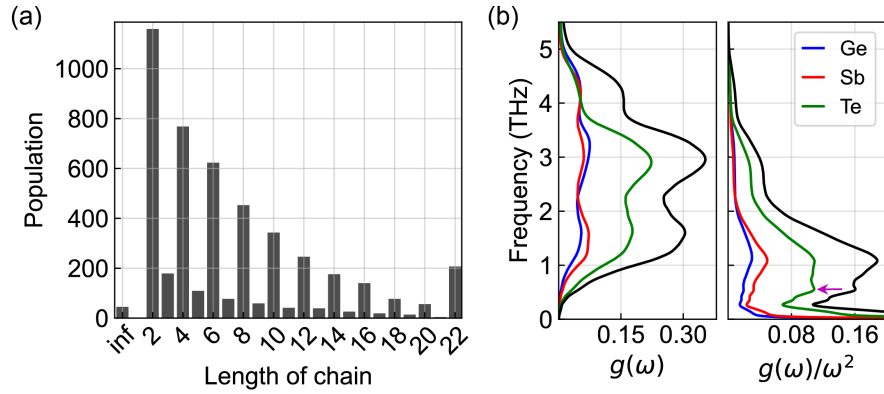


Fig. S12. The (a) p -bonding chain length histogram and (b) VDOS calculated by VACF of c-GST at 300 K crystallized from a-GST. A melt-quenched a-GST was crystallized by heating of 200 ps long from 300 K to 700 K followed by annealing of 300 ps long at 700 K and cooling of 50 ps long to 300 K. A c-GST seed consisting of 2053 atoms was attached to a-GST to aid single-domain crystallization. An equilibrium NVT-MD (300 K) was simulated to calculate VDOS in (b). The purple arrow in (b) highlights the boson peak at 0.560 THz.

Lattice thermal conductivity calculated by Müller-Plathe rNEMD simulation

The lattice thermal conductivity of c-GST with various vacancy distributions was calculated using the reverse nonequilibrium molecular dynamics (rNEMD) method. This rNEMD method is based on the macroscopic definition of thermal conductivity $J_x = -\kappa_{xx} \frac{\partial T}{\partial x}$, where J_x is the heat current, κ_{xx} is a diagonal component of the lattice thermal conductivity tensor, and $\partial T / \partial x$ is the temperature gradient along the x -axis. In this approach, the lattice thermal conductivity is obtained from the ratio of the thermal gradient to the manually built heat current. The Müller-Plathe method is a simple and powerful rNEMD algorithm that satisfies the necessary conditions for steady-state ensembles, especially the laws of energy and momentum conservation [3].

The simulation box was evenly partitioned into $2N$ slabs in the direction of interest, with the momentum of the hottest atom in the first slab and the coldest atom in the $(N + 1)$ -th slab being exchanged periodically with a constant time interval [3]. When a steady state is established by the thermal flux inside the simulation box and manual energy exchange after a long enough simulation, the lattice thermal conductivity can readily be calculated [3]. The rNEMD simulations based on the Müller-Plathe method in this study were implemented using the LAMMPS package [4].

We investigated the effect of vacancy ordering in c-GST on lattice thermal conductivity. We chose the configurations at 10 ps and 100 ns and calculated the lattice thermal conductivity using 300 K rNEMD simulations. The configurations at 10 ps and 100 ns were partitioned into 24 equal-sized slabs along the x -direction. The virtual heat flux was established by cooling the first slab as a heat sink at -4 eV/ps and heating the thirteenth slab as a heat source at 4 eV/ps. An initial 50 ps-long rNEMD simulation was conducted to establish a steady state with the virtual heat flux, followed by a 1 ns-long rNEMD simulation, from which the temperature profile was sampled (Fig. S13). The temperature gradient was calculated using the least-square regression function from the SciPy package [5] in the regions showing linear temperature slopes (slabs 4~10 and 16~22, Fig. S13). The lattice thermal conductivities calculated by the non-stochastic rNEMD method were 0.41 W/mK and 0.40 W/mK for the 10 ps and 100 ns configurations, respectively. This result indicates that lattice thermal conductivity in c-GST is insensitive to vacancy distribution, which is consistent with experimentally indistinguishable

lattice thermal conductivities between c-GST and h-GST [6-9]. The room-temperature lattice thermal conductivities of c-GST and h-GST were measured as 0.4~0.5 W/mK [6-9]. The lattice thermal conductivity of h-GST is high in the in-plane direction but low in the out-of-plane direction due to the periodic array of vdW gaps [10]. As a result, the average lattice thermal conductivity of h-GST is similar to that of c-GST with a complex vacancy distribution. Our calculated lattice thermal conductivity using the Müller-Plathe method was 0.42 W/mK for both the 10 ps and 100 ps configurations.

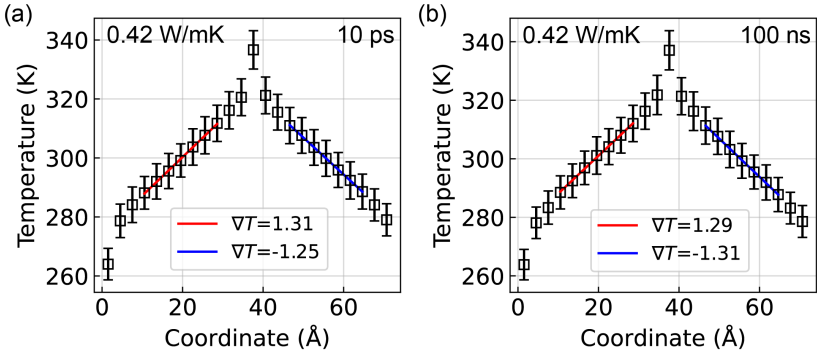


Fig. S13. Temperature profile along the *a*-direction of (a) 10 ps and (b) 100 ns configurations from 300 K Müller-Plathe rNEMD simulations. The vertical bars indicate the standard deviation of slab temperatures for 1 ns, where the slab temperature at a time point was measured every 1 ps by averaging temperatures of the past 1 ps. The coldest atom in slab 13 and the hottest atom in slab 1 were exchanged every 50 fs, which formed an effective thermal flux of ~3.50 eV/ps between the slabs 1 and 13.

References

- [1] Y.-S. Song, J. Kim, and S.-H. Jhi, Phonon Instability and Broken Long-Ranged p Bond in Ge-Sb-Te Phase-Change Materials from First Principles, *Phys. Rev. Appl.* **9**, 054044 (2018).
- [2] Y. M. Beltukov, C. Fusco, A. Tanguy, and D. A. Parshin, Transverse and longitudinal vibrations in amorphous silicon, *J. Phys.: Conf. Ser.* **661**, 012056 (2015).
- [3] F. Müller-Plathe, A simple nonequilibrium molecular dynamics method for calculating the thermal conductivity, *J. Chem. Phys.* **106**, 6082-6085 (1997).
- [4] A. P. Thompson, H. M. Aktulga, R. Berger, D. S. Bolintineanu, W. M. Brown, P. S. Crozier, P. J. in 't Veld, A. Kohlmeyer, S. G. Moore, T. D. Nguyen, *et al.*, LAMMPS - a flexible simulation tool for particle-based materials modeling at the atomic, meso, and continuum scales, *Comput. Phys. Commun.* **271**, 108171 (2022).
- [5] P. Virtanen and R. Gommers and T. E. Oliphant and M. Haberland and T. Reddy and D. Cournapeau and E. Burovski and P. Peterson and W. Weckesser and J. Bright, *et al.*, SciPy 1.0: fundamental algorithms for scientific computing in Python, *Nat. Methods* **17**, 261-272 (2020).
- [6] H.-K. Lyeo, D. G. Cahill, B.-S. Lee, J. R. Abelson, M.-H. Kwon, K.-B. Kim, S. G. Bishop, and B.-k. Cheong, Thermal conductivity of phase-change material $\text{Ge}_2\text{Sb}_2\text{Te}_5$, *Appl. Phys. Lett.* **89**, 151904 (2006).
- [7] J. Lee, E. Bozorg-Grayeli, S. Kim, M. Asheghi, H. S. Philip Wong, and K. E. Goodson, Phonon and electron transport through $\text{Ge}_2\text{Sb}_2\text{Te}_5$ films and interfaces bounded by metals, *Appl. Phys. Lett.* **102**, 191911 (2013).
- [8] E. K. Kim, S. I. Kwun, S. M. Lee, H. Seo, and J. G. Yoon, Thermal boundary resistance at $\text{Ge}_2\text{Sb}_2\text{Te}_5/\text{ZnS}:\text{SiO}_2$ interface, *Appl. Phys. Lett.* **76**, 3864-3866 (2000).
- [9] C. Peng, L. Cheng, and M. Mansuripur, Experimental and theoretical investigations of laser-induced crystallization and amorphization in phase-change optical recording media, *J. Appl. Phys.* **82**, 4183-4191 (1997).
- [10] D. Campi, L. Paulatto, G. Fugallo, F. Mauri, and M. Bernasconi, First-principles calculation of lattice thermal conductivity in crystalline phase change materials: GeTe , Sb_2Te_3 , and $\text{Ge}_2\text{Sb}_2\text{Te}_5$, *Phys. Rev. B* **95**, 024311 (2017).